Met. Mater. Int., Vol. 20, No. 4 (2014), pp. 577~583
doi: 10.1007/s12540-014-4001-6

Design of Cost-Effective Fe-Based Amorphous Coating Alloys Having High Amorphous Forming Ability by Thermodynamic Calculation

Seungmun Jung[1], Jeonghyeon Do[2], Dong-Geun Lee[3], Byeong-Joo Lee[1], Gil-up Cha[4], and Sunghak Lee[1,*]

[1]Pohang University of Science and Technology, Center for Advanced Aerospace Materials, Pohang, 790-784, Korea
[2]Korea Institute of Materials Science, Advanced Metallic Materials Division, Changwon, 642-831, Korea
[3]Korea Institute of Materials Science, Light Metal Division, Changwon, 642-831, Korea
[4]POSCO, Rolling Facilities Group, Pohang Works, Pohang, 790-785, Korea

(received date: 27 June 2013 / accepted date: 26 November 2013)

In this study, new cost-effective Fe-based amorphous coating alloys having high amorphous forming ability were developed by varying the Fe content, while their microstructure, hardness, and corrosion resistance were also evaluated. Chemical compositions that have the lowest driving force of formation of crystalline phases such as Fe_3P, Fe_3C, and α-Fe were obtained from thermodynamically calculated phase diagrams of the representative $Fe_xAl_2(P_{10.83}C_{7.47}B_{1.7})_{98-x}$ alloy system at a crystallization temperature of 443 °C. Considering the intersections of driving force curves of Fe_3P and Fe_3C, Fe_3P and α-Fe, and Fe_3C and α-Fe, the Fe contents were found to be 77.8, 76.2, and 75.8 at.%, respectively. The microstructural analysis results of 1.5-mm-diameter suction-cast Fe-based alloys indicated that the $Fe_{76.5}Al_2(P_{10.83}C_{7.47}B_{1.7})_{21.5}$ alloy had a fully amorphous microstructure, whereas crystalline phases were formed in other alloys. This alloy showed a better hardness and corrosion resistance than conventional thermal spray coating alloys, and its production cost could also be reduced by using less expensive alloying elements, which could provide a good way to practically apply this alloy to Fe-based amorphous thermal spray coatings.

Keywords: amorphous materials, driving force of formation, casting, phase transformation, microstructure

1. INTRODUCTION

In general, amorphous alloys have excellent properties of strength, stiffness, and corrosion resistance because of their distinctive liquid-like structure [1,2]. However, the manufacturing cost is still high because of the relatively high expense of alloying elements and the requirement of a vacuum environment during the casting. The size and shape of alloy products are also quite restricted [3,4]. When amorphous alloys that do not have dislocations inside are deformed, shear bands play an important role in initiating deformation and fracture, thereby leading to an abrupt fracture in a shear mode [5]. This brittle fracture works as an obstacle to good reliability in the life of high-performance components. If amorphous/metal coatings, in which the surface consists of an amorphous alloy and the interior substrate consists of a ductile metal, can be successfully developed, these problems of high manufacturing cost and brittle fracture can be solved simultaneously.

A number of ferrous amorphous coatings have been fabricated by thermal spraying methods such as high velocity oxyfuel (HVOF) because of the ready formation of amorphous phases when completely molten ferrous amorphous powders are contacted with a substrate at very fast cooling rates [6,7]. According to the recent results of ferrous Fe-Cr-based amorphous coatings [8], the coatings could be successfully fabricated by the low-pressure plasma spraying technique by applying them to the surface treatment of various parts such as boilers, pumps, impellers, and pulleys in power generation industries. However, these coating alloys were somewhat expensive because they contained a considerable amount of expensive alloying elements of Co, Ni, or Cr. Thus, the fabrication idea of ferrous amorphous coating alloys that are cost-effective and have sufficiently high amorphous forming ability is quite useful for applications of their thermal spray coatings in various industrial areas, while fully taking advantage of amorphous alloys.

In this study, new cost-effective Fe-based amorphous coating alloys that have high glass formability were developed. Chemical compositions of super-cooled liquid that have the lowest driving force for forming crystalline phases such as Fe_3P, Fe_3C, and α-Fe were obtained from thermodynamically calculated phase diagrams of the Fe-Al-P-C-B five-component system [9,10]. In order to match these driving force data

*Corresponding author: shlee@postech.ac.kr

with the experimental data of actual phase formation, the experiments of casting and phase analysis were performed, and then the microstructure, hardness, and corrosion resistance of the cast alloys were investigated. The appropriate compositions of cost-effective Fe-based amorphous alloys for thermal spray coatings were suggested.

2. EXPERIMENTAL PROCEDURE

Since Fe-based amorphous alloys are of a disordered phase that consists of metal and metalloid elements in atomic levels, the ratio of metallic and metalloid elements is important in determining the amorphous forming ability. P, C, and B were added as main metalloid elements in this study. The addition of C and P was inevitable for improving the amorphous forming ability without adding expensive alloying elements [11]. A small amount (about 2 at.%) of Al was also added to improve the amorphous forming ability because Al expands the supercooled liquid zone [12]. The amount of B was determined to be 1.7 at.%, considering the high price of the Fe-B alloy. The representative alloy composition having a Fe-Al-P-C-B component system was $Fe_{78}Al_2P_{10.83}C_{7.47}B_{1.7}$ according to the previous research [13]. Furthermore, in order to improve the amorphous forming ability, Fe and metalloid elements of P, C, and B were varied to determine the better alloy composition of $Fe_xAl_2(P_{10.83}C_{7.47}B_{1.7})_{98-x}$. In addition, the formation behavior of Fe_3C and Fe_3P having a high driving force for formation was analyzed in detail by thermodynamic calculations [14].

Master alloys (weight: about 25 g) were made by arc-melting appropriate amounts of pure metals of Fe (99.9%), Al (99.99%), and C (99%) and ferroalloys of Fe-B (99.2%) and Fe-P (99.8%) in a water-cooled copper crucible under a Ti-gettered argon atmosphere. Rods of 1.2 mm or 1.5 mm in diameter and 50 mm in length (weight: about 0.4 g or 0.5 g) were fabricated in a water-cooled copper mold by suction casting under an argon atmosphere. The suction-cast alloys were polished in diamond pastes (size: 0.25 mm), etched by a Vilella's solution (45 ml Glycerol, 15 ml HNO_3, and 30 ml HCl), and observed by a scanning electron microscope (SEM, model: JSM-6330F, Jeol, Japan). Phases present in the alloys were analyzed by X-ray diffraction (XRD, Cu radiation, scan rate: 2 deg·min^{-1}; scan step size,: 0.02 deg; angle range: 20 deg ≤ 2θ ≤ 100 deg). Hardness was measured by a Vickers hardness tester under a 100 g load.

Open circuit potential (OCP) measurements and potentiodynamic polarization tests were conducted in an aerated 1% NaCl solution at room temperature. A saturated calomel electrode (SCE) was used as a reference electrode, and two parallel high-density graphite rods were served as counter electrodes for the current measurement. Suction-cast Fe-base amorphous alloy specimens (rod shape) were mounted by a nonconductive macromolecule resin so that they could be connected to electrodes [14]. The OCP was measured after a delay of 30 minutes for the specimens to reach a steady state. Then, the specimen was potentiodynamically polarized at a scan rate of 0.0004 V/s from -0.25 V below the OCP to +1.2 V above the SCE potential.

3. RESULTS AND DISCUSSION

3.1. Thermodynamic calculation of driving force of formation of crystalline phases

Thermodynamic calculations were conducted to find alloy compositions with high amorphous forming ability. Here, a composition of super-cooled liquid with the lowest driving force of formation for other crystalline phases was selected. The ThermoCalc software was used for calculation, and the upgraded version of TCFE2000 was used for the thermodynamic database [16-18]. In this database, Fe_3P was considered as a stoichiometric compound [18], but the experimental information showed a non-negligible solubility of B replacing P sites [19]. Thus, the thermodynamic model for Fe_3P was extended to $Fe_3(P,B)$ to represent the solubility of B [19].

The differential scanning calorimetry (DSC) analysis was conducted on the representative alloy composition ($Fe_{78}Al_2P_{10.83}C_{7.47}B_{1.7}$) to determine the temperature, which is one of the important parameters for calculating the driving force of phase formation. Figure 1 shows a thermogram of the alloy at a heating rate of 10 °C/min. From this thermogram, the glass transition temperature (T_g) and crystallization temperature ($T_{x,onset}$) were measured to be 417 °C and 443 °C, respectively.

Figure 2 shows the driving force curves of formation of Fe_3P, Fe_3C, α-Fe, $Fe_{23}C_6$, and γ-Fe and in the $Fe_xAl_2(P_{10.83}C_{7.47}B_{1.7})_{98-x}$ alloy system at 443 °C as a function of atomic

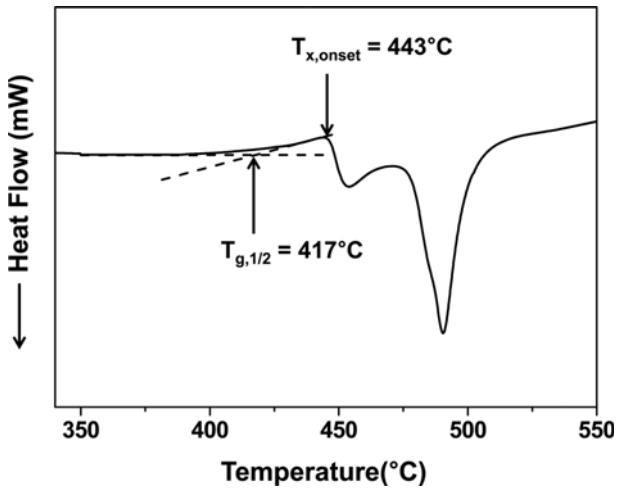

Fig. 1. Differential scanning calorimetry (DSC) thermogram of the representative alloy ($Fe_{78}Al_2P_{10.83}C_{7.47}B_{1.7}$ (at.%), 78Fe alloy) at a heating rate of 10 °C/min. The glass transition temperature (T_g) and crystallization temperature ($T_{x,onset}$) are 417 °C and 443 °C, respectively.

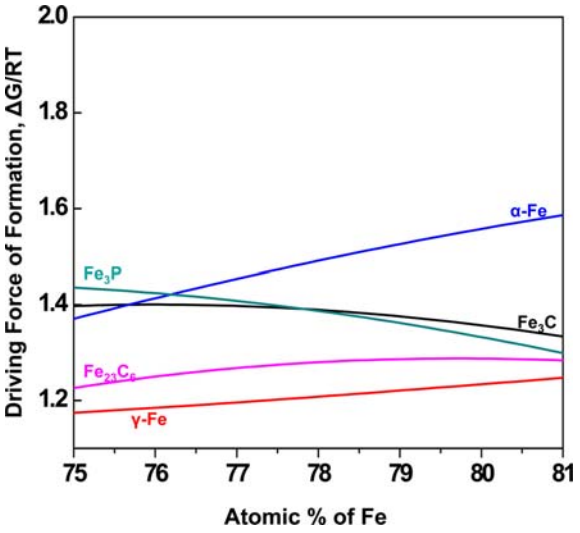

Fig. 2. Driving force curves of formation of Fe_3P, Fe_3C, α-Fe, $Fe_{23}C_6$, and γ-Fe in the $Fe_xAl_2(P_{10.83}C_{7.47}B_{1.7})_{98-x}$ alloy system at 443 °C as a function of atomic fraction of Fe. These curves were calculated by an analysis program of ThermoCalc on the basis of the upgraded version of TCFE2000 [18].

fraction of Fe. The driving forces of formation of Fe_3P, Fe_3C, and α-Fe are relatively high, while those of $Fe_{23}C_6$ and γ-Fe are low. This indicates that the possibility of forming Fe_3P, Fe_3C, and α-Fe phases is high in the $Fe_xAl_2(P_{10.83}C_{7.47}B_{1.7})_{98-x}$ alloy system.

In order to match these driving force data with the experimental data of actual phase formation, the preliminary experiments of casting and phase analysis were performed. Five Fe-based alloys, whose Fe contents were varied at 76, 77, 78, 78.5, and 79 at.%, were made into a rod shape (diameter: 1.2 mm; length: 50 mm) by suction casting. Figure 3 shows the X-ray diffraction (XRD) analysis data of the five alloys. Many peaks of crystalline phases can be observed in the 78.5Fe-Al-P-C-B and 79Fe-Al-P-C-B alloys, but disappear as the Fe content decreases. These XRD data indicate that only phases of Fe_3P, Fe_3C, and α-Fe are formed without $Fe_{23}C_6$ and γ-Fe phases in the $Fe_xAl_2(P_{10.83}C_{7.47}B_{1.7})_{98-x}$ alloy system. This is because the actual driving forces for forming $Fe_{23}C_6$ and γ-Fe phases might have been reduced below the calculated driving forces by some reasons or factors that were not considered in the thermodynamic calculation [20]. For example, $Fe_{23}C_6$ carbides kinetically need a long time for their precipitation because they have a large and complicated unit cell of a square antiprism shape [21,22]. Thus, driving force curves for the formation of $Fe_{23}C_6$ and γ-Fe phases are eliminated from Fig. 2, as shown in Fig. 4. Considering both driving force curves of Fe_3P and Fe_3C, the intersection of the two curves indicates the composition (X = 77.8) at which driving forces of Fe_3P and Fe_3C are minimized while the possibility of forming amorphous phases is maximized. From the compositions located at curve intersections, *e.g.*, Fe_3P and Fe_3C, Fe_3P and α-Fe,

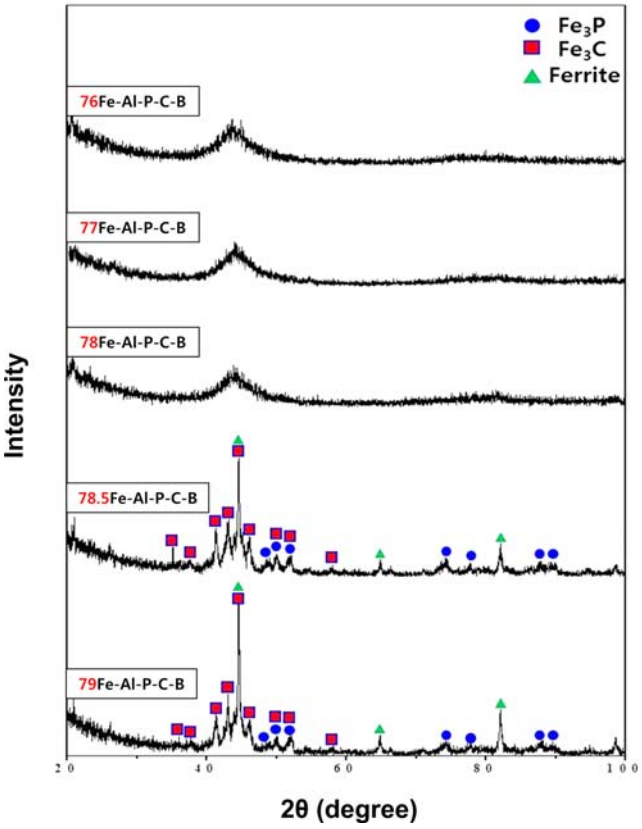

Fig. 3. X-ray diffraction (XRD) patterns of the five Fe-based alloys, whose Fe contents were varied at 76, 77, 78, 78.5, and 79 at.%, in the $Fe_xAl_2(P_{10.83}C_{7.47}B_{1.7})_{98-x}$ alloy system, showing peaks of Fe_3P, Fe_3C, and α-Fe as well as hallow patterns of amorphous phase. The Fe-based alloys were made in a rod shape (diameter; 1.2 mm, length; 50 mm) by suction casting.

and Fe_3C and α-Fe, the Fe contents were selected to be 77.8, 76.2, and 75.8 at.%, respectively, as indicated by arrows in Fig. 4. According to this thermodynamic calculation, together with the XRD data of Fig. 3, the final alloy compositions at which the amorphous forming ability is maximized are determined to be $Fe_xAl_2(P_{10.83}C_{7.47}B_{1.7})_{98-x}$ ($76 \le X \le 78$).

3.2. Microstructure of Suction-Cast $Fe_xAl_2(P_{10.83}C_{7.47}B_{1.7})_{98-x}$ Alloys

The Fe-based alloys having compositions of $Fe_xAl_2(P_{10.83}C_{7.47}B_{1.7})_{98-x}$ ($76 \le X \le 78$), *i.e.*, $Fe_{76}Al_2(P_{10.83}C_{7.47}B_{1.7})_{22}$, $Fe_{76.5}Al_2(P_{10.83}C_{7.47}B_{1.7})_{21.5}$, $Fe_{77}Al_2(P_{10.83}C_{7.47}B_{1.7})_{21}$, $Fe_{77.5}Al_2(P_{10.83}C_{7.47}B_{1.7})_{20.5}$, and $Fe_{78}Al_2(P_{10.83}C_{7.47}B_{1.7})_{20}$), were made in a rod shape (diameter: 1.5 mm; length: 50 mm) by suction casting. For convenience, Fe-based alloys having compositions of $Fe_{76}Al_2(P_{10.83}C_{7.47}B_{1.7})_{22}$, $Fe_{76.5}Al_2(P_{10.83}C_{7.47}B_{1.7})_{21.5}$, $Fe_{77}Al_2(P_{10.83}C_{7.47}B_{1.7})_{21}$, $Fe_{77.5}Al_2(P_{10.83}C_{7.47}B_{1.7})_{20.5}$, $Fe_{78}Al_2(P_{10.83}C_{7.47}B_{1.7})_{20}$ are referred to as 76Fe, 76.5Fe, 77Fe, 77.5Fe, and 78Fe alloys, respectively, according to the Fe content (X). Here, the 78Fe alloy has a representative alloy composition as forementioned in the Experimental section.

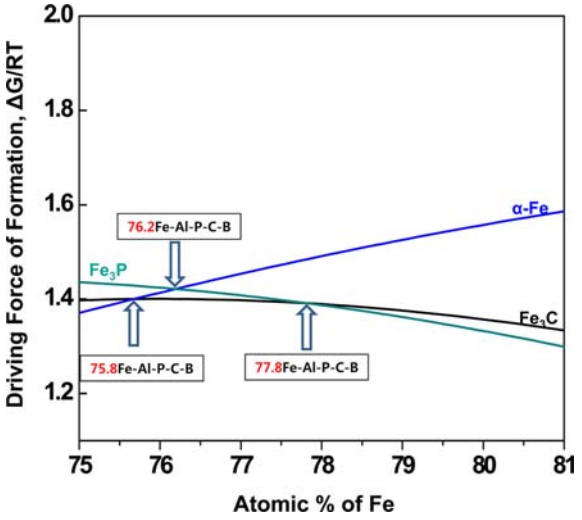

Fig. 4. Driving force curves of formation of Fe_3P, Fe_3C, and α-Fe in the $Fe_xAl_2(P_{10.83}C_{7.47}B_{1.7})_{98-x}$ alloy system at 443 °C as a function of atomic fraction of Fe. From the compositions located at curve intersections, *e.g.*, Fe_3P and Fe_3C, Fe_3P and α-Fe, and Fe_3C and α-Fe, the Fe contents are selected to be 77.8, 76.2, and 75.8 at.%, respectively, as indicated by arrows.

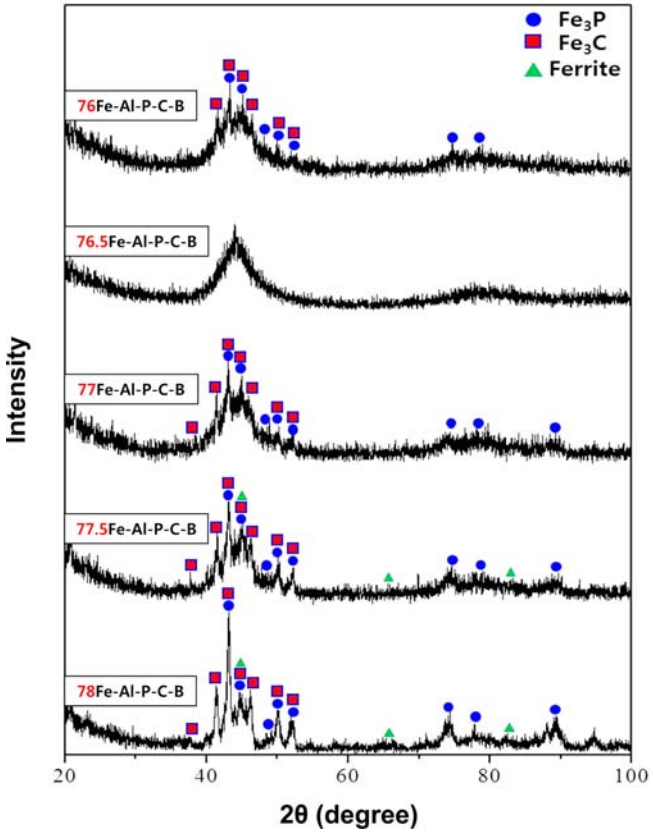

Fig. 5. X-ray diffraction (XRD) patterns of the five Fe-based alloys, whose Fe contents were varied at 76, 76.5, 77, 77.5, and 78 at.%, in the $Fe_xAl_2(P_{10.83}C_{7.47}B_{1.7})_{98-x}$ alloy system, showing peaks of Fe_3P, Fe_3C, and α-Fe as well as hallow patterns of amorphous phase. The Fe-based alloys were made in a rod shape (diameter; 1.5 mm, length; 50 mm) by suction casting.

Figure 5 shows the XRD analysis data of the five alloys. Peaks of Fe_3P and Fe_3C, as well as hollow patterns of amorphous phase, are found in the 76Fe and 77Fe alloys, but only broad patterns are observed in the 76.5Fe alloy. In the 77.5Fe and 78Fe alloys containing a high content of Fe, peaks of Fe_3P, Fe_3C, and α-Fe appear together with hallow patterns. These XRD data are different from the XRD data shown in Fig. 5 because the cooling rate of 1.5-mm-diameter suction-cast rods is slower than that of 1.2-mm-diameter suction-cast rods. In the case of the 78Fe alloy, for example, peaks of crystalline phases are not found in the XRD data of the 1.2-mm-diameter rods (Fig. 3), but they are found in the XRD data of the 1.5-mm-diameter rods (Fig. 5). This indicates that the 1.5-mm-diameter rods need a higher amorphous forming ability than 1.2-mm-diameter rods.

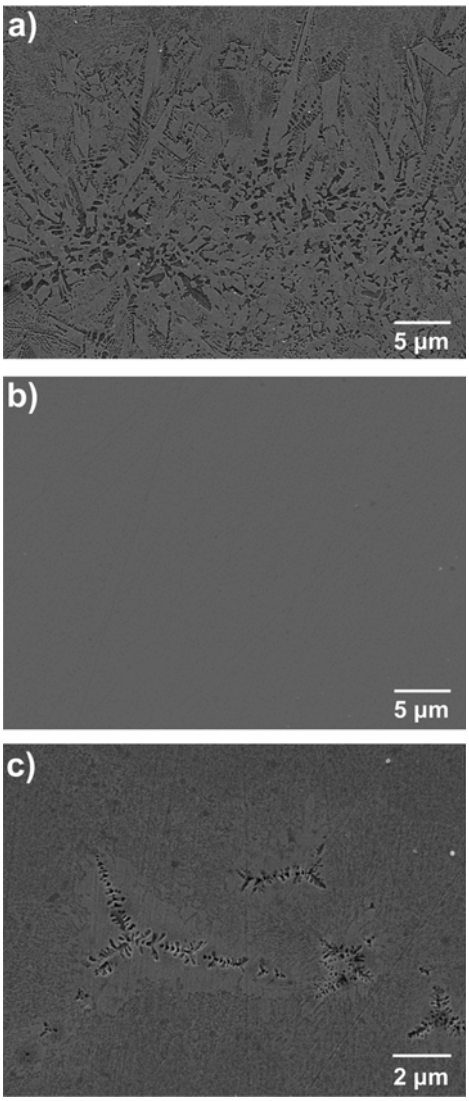

Fig. 6. SEM micrographs of the (a) 76Fe alloy ($Fe_{76}Al_2(P_{10.83}C_{7.47}B_{1.7})_{22}$), (b) 76.5Fe alloy ($Fe_{76.5}Al_2(P_{10.83}C_{7.47}B_{1.7})_{21.5}$), and (c) 78Fe alloy ($Fe_{78}Al_2(P_{10.83}C_{7.47}B_{1.7})_{20}$)), showing crystalline phases in the amorphous matrix of the 76Fe and 78Fe alloys.

SEM microstructures of 1.5-mm-diameter suction-cast rods of the 76Fe, 76.5Fe, and 78Fe alloys are shown in Fig. 6(a) through (c). In the 76Fe and 78Fe alloys, crystalline phases are found in a dendritic shape (Fig. 6(a) and Fig. 6(c)), whereas they are not observable in the 76.5Fe alloy (Fig. 6(b)). This indicates that the amorphous forming ability is improved in the 76.5Fe alloy in comparison with the 76Fe or 78Fe alloy. It is also noted that the amorphous microstructure of the 76.5Fe alloy matches the thermodynamically calculated data at 443 °C of Fig. 4, *i.e.*, the composition (X=76.2) located at the curve intersections of Fe_3P and α-Fe, whereas those of the 76Fe and 78Fe alloys are not matched because the 76Fe and 78Fe alloys contain crystalline phases. The main reason for the unmatched microstructure with the thermodynamically calculated data is due to the importance of the formation of crystalline phases because the actual driving forces for formingFe_3P and α-Fe phases might be quite above the calculated driving forces. Thus, the driving force for the formation of Fe_3P and α-Fe is useful for estimating the amorphous forming ability of the present alloy system.

3.3. Hardness and Corrosion Resistance of Suction-Cast $Fe_xAl_2(P_{10.83}C_{7.47}B_{1.7})_{98-x}$ Alloys

The Vickers hardness values of the 76Fe, 76.5Fe, 77Fe, 77.5Fe, and 78Fe alloys are 1084, 1099, 1081, 1060, and 1061 VHN, respectively. These hardness values show higher hardness than those of conventional thermal spray coating alloys [8,23]. The 76.5Fe alloy composed of amorphous phase shows slightly higher hardness than the other alloys containing crystalline phases. The hardness of the five alloys is higher than 1000 VHN, and the hardness difference between the alloys is not large because the crystalline phases of Fe_3P and Fe_3C are hard.

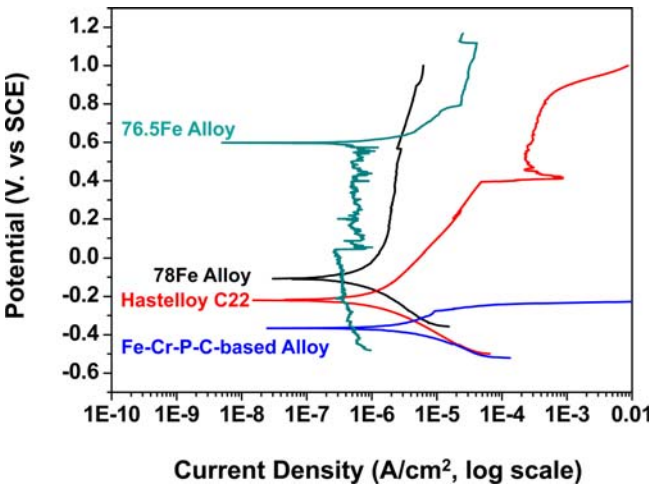

Fig. 7. Potentiodynamic polarization curves of the 76.5Fe alloy, 78Fe alloy, Fe-Cr-P-C-based alloy (composition; Fe-10Cr-13P-7C (at.%)), and hastelloy C22 alloy (composition; Ni-22Cr-13Mo-3.0Fe-3.0W-2.5Co-0.5Mn-0.35V-0.08Si-0.01C (wt.%)). The test specimen of the 76.5Fe alloy was obtained from a 1.5-mm-diameter suction-cast rod, whereas those of the 78Fe alloy and Fe-Cr-P-C-based alloy were obtained from 1.2-mm-diameter suction-cast rods. The specimens were immersed in a 1% NaCl solution at room temperature.

Figure 7 shows potentiodynamic polarization curves of the 76.5Fe alloy, 78Fe alloy, Fe-Cr-P-C-based alloy (composition: Fe-10Cr-13P-7C (at.%)) [8], and hastelloy C22 alloy (composition: Ni-22Cr-13Mo-3.0Fe-3.0W-2.5Co-0.5Mn-0.35V-0.08Si-0.01C (wt%)), which are commercially used as thermal spray coating alloys [24]. The test specimen of the 76.5Fe alloy was obtained from a 1.5-mm-diameter suction-cast rod, whereas those of the 78Fe alloy and Fe-Cr-P-C-based alloy were obtained from 1.2-mm-diameter suction-cast rods. Thus, both the 76.5Fe and 78Fe alloy specimens consist of amorphous phases (Fig. 3 and Fig. 5), but the Fe-Cr-P-C-based alloy contains some crystalline phases because of its low amorphous forming ability [8].

The corrosion potential (E_o) and corrosion current density (i_o) were obtained from the polarization curves, and the results are shown in Table 1. These results do not represent the absolute values because the modified potentiodynamic polarization test is not a standard corrosion test. However, this test provides a relative comparison of corrosion resistance [25]. The corrosion current density was measured from the intersecting points of two Tafel lines of polarization curves. i_o of the 76.5Fe alloy is lower than that of the 78Fe alloy, Fe-Cr-P-C-based alloy, and the hastelloy C22. E_o is also the highest of the 76.5Fe alloy. It can be concluded from the data of i_o and E_o that the corrosion resistance of the 76.5Fe alloy is the best among the alloys. This can be attributed to the full amorphous microstructure, in which grain boundaries do not exist [1]. When the 76.5Fe and 78Fe alloys composed of amorphous phases are compared, the 76.5Fe alloy has a better corrosion resistance than the 78Fe alloy. These results imply that the better amorphous forming ability leads to a better corrosion resistance, even in amorphous alloys.

The relative price percentages of alloying elements contained in the alloys were estimated on the basis of the price of the 76.5Fe alloy, and the results are shown in Table 1. These standard prices were estimated by prices of ferroalloys of the LME (London Metal Exchange) daily price (date: June 25th, 2013) [26,27]. The price of alloying elements contained in the 76.5Fe alloys is lower than that contained in the Fe-Cr-P-C-based alloy, while it is similar to that of the 78Fe alloy. It is also much lower than that contained in the hastel-

Table 1. Potentiodynamic polarization test results and relative price percentage of the 76.5Fe alloy, 78Fe alloy, Fe-Cr-P-C-based alloy, and hastelloy C22

Alloy	E_0 (V_{SCE})	i_0 (μA/cm^2)	Relative Price Percentage (%)
76.5Fe Alloy	0.598	0.108	100
78Fe Alloy	-0.108	0.156	96
Fe-Cr-P-C-based Alloy	-0.366	2.497	115
Hastelloy C22	-0.220	0.720	1632

loy C22. This implies that the commercially used Fe-Cr-P-C-based alloy or hastelloy 22 can be sufficiently replaced by the 76.5Fe alloy.

The present study on the development of cost-effective Fe-based amorphous alloys by modifying conventional Fe-based alloys can be a good way to apply these alloys to amorphous thermal spray coatings. It can also be useful to understand the behavior of amorphous forming ability and to suggest optimal alloy compositions for improving amorphous forming ability. The 76.5Fe alloy consists of a full amorphous phase, and shows the best hardness and corrosion resistance. Its wear resistance could be excellent when its high hardness was considered, although the wear test was not conducted in this study. These results are outstanding ones, which have been hardly reported in previous studies on Fe-based amorphous alloys, and the improvement of amorphous forming ability is explained by thermodynamically calculated phase diagrams that achieve an alloy composition having the lowest driving force for forming crystalline phases. In order to further improve the microstructures and properties of Fe-based amorphous alloys, intensive studies to select or develop new alloy compositions for enhancing the amorphous forming ability and to clarify mechanisms involved in improved hardness and resistance to wear or corrosion should continue.

4. CONCLUSIONS

In this study, cost-effective Fe-based amorphous alloys used for thermal spray coatings were developed by varying the Fe content, and their microstructure, hardness, and corrosion resistance were investigated.

(1) Based on the representative $Fe_xAl_2(P_{10.83}C_{7.47}B_{1.7})_{98-x}$ alloy system at the crystallization temperature of 443 °C, the Fe content was varied to calculate the driving force of the formation of crystalline phases of Fe_3P, Fe_3C, α-Fe, $Fe_{23}C_6$, and γ-Fe by using the thermodynamic database. The preliminary calculation results showed that only phases of Fe_3P, Fe_3C, and α-Fe were formed in this alloy system. Considering the intersections of driving force curves of Fe_3P and Fe_3C, Fe_3P and α-Fe, and Fe_3C and α-Fe, the Fe contents were selected to be 77.8, 76.2, and 75.8 at.%, respectively.

(2) The microstructural analysis results of 1.5-mm-diameter suction-cast Fe-based alloys indicated that the $Fe_{76.5}Al_2(P_{10.83}C_{7.47}B_{1.7})_{21.5}$ alloy (76.5Fe) had a fully amorphous microstructure, whereas crystalline phases such as Fe_3P, Fe_3C, and α-Fe were formed in the $Fe_{76}Al_2(P_{10.83}C_{7.47}B_{1.7})_{22}$ alloy (76Fe) and $Fe_{78}Al_2(P_{10.83}C_{7.47}B_{1.7})_{20}$ alloy (78Fe). These results were well matched with the thermodynamically calculated data. Thus, the calculated driving force for the formation of crystalline phases was useful for estimating the amorphous forming ability of Fe-based alloys.

(3) The 76.5Fe alloy had a completely amorphous microstructure with a maximum thickness of 1.5 mm at least, and showed better hardness and corrosion resistance than conventional thermal spray coating alloys. The improvement in amorphous forming ability was explained by thermodynamically calculated phase diagrams to achieve an alloy composition that has the lowest driving force in the formation of crystalline phases. Its production cost could also be reduced by using less expensive alloying elements, which could provide a good way to practically apply Fe-based amorphous thermal spray coatings.

ACKNOWLEDGMENTS

This work was supported by POSCO under a contract No. 2010Y114. The authors would like to thank Dr. Hyung-Jun Kim and Jin Hong Kim of Research Institute of Industrial Science and Technology (RIST) and Mr. Hyuk-Joong Lee for their help with fabrication of the Fe-based amorphous alloys.

REFERENCES

1. A. Inoue, *Acta Mater*. **48**, 279 (2000).
2. V. Ponnambalam, S. J. Poon, G. J. Shiflet, V. M. Keppens, R. Taylor, and G. Petculescu, *Appl. Phys. Lett.* **83**, 1131 (2003).
3. Z. P. Lu and C. T. Liu, *Acta Mater*. **50**, 3501 (2002).
4. A. Inoue, W. Zhang, T. Zhang, and K. Kurosaka, *Acta Mater*. **29**, 2645 (2001).
5. W. L. Johnson, *MRS Bull*. **24**, 42 (1999).
6. H. Kim, K. Lim, B. Seong, and C. Park, *J. Mater. Sci*. **36**, 49 (2001).
7. S. L. Wang, H. X. Li, S. Y. Hwang, S. D. Choi, and S. Yi, *Met. Mater. Int*. **18**, 607 (2012)
8. K. Kishitake, H. Era, and F. Otsubo, *J. Therm. Spray Technol*. **5**, 476 (1996).
9. A. Inoue and J. S. Gook, *Mater. Trans. JIM*. **36**, 1180 (1995).
10. H. Li and S. Yi, *Mater. Sci. Eng*. **A449**, 189 (2007).
11. Y. Wu, X. D. Hui, Z. P. Lu, Z. Y. Liu, L. Liang, and G. L. Chen, *J. Alloys Compd*. **467**, 187 (2009).
12. A. Inoue, A. Takeuchi, and T. Zhang, *Metall. Mater. Trans. A* **29A**, 1779 (1998).
13. J. Do, S. Jung, H.-J. Lee, B.-J. Lee, G.-U. Cha, C. Y. Jo, and S. Lee, *Metall. Mater. Trans*. A **44A**, 2573 (2013).
14. M. G. Scott and P. Ramachandrarao, *Mater. Sci. Eng*. **A29**, 137 (1977).
15. Z. Long, Y. Shao, G. Xie, P. Zhang, B. Shen, and A. Inoue, *J. Alloys Compd*. **462**, 52 (2008).
16. B. Sundman, B. Jansson, and J.-O. Andersson, *Calphad*. **9**, 153 (1985).
17. TCFE2000, The Thermo-Calc Steels Database, upgraded by B.-J. Lee, B. Sundman at KTH, Stockholm (1999).
18. B.-J. Lee, Pohang University of Science and Technology (POSTECH), Korea, unpublished update of thermodynamic database.

19. V. Raghavan, *Phase Diagrams of Ternary Iron Alloys, Indian Institute of Metals*, Calcutta (1988).
20. M. Tavoosi, F. Karimzadeh, M. H. Enayati, S. Lee, and H. S. Kim, *Met. Mater. Int*. **19**, 901 (2013).
21. D. H. Jack and K. H. Jack, *Mater. Sci. Eng.* **11**, 1 (1973).
22. J. D. Robson and H. K. D. H. Bhadeshia*, Calphad*. **20**, 447 (1996).
23. M. Komaki, T. Mimura, R. Kurahasi, M. Kouzaki, and T. Yamasaki, *Mater, Trans. JIM*. **52**, 474 (2011).
24. T. E. Lister, R. N. Wright, P. J. Pinhero, and W. D. Swank, *J. Therm. Spray Technol*. **11**, 530 (2002).
25. M. Kim, S. Kim, S. Yoon, and S. Yi, *Korean. J. Met. Mater.* **52**, 129 (2014).
26. London Metal Exchange, http://www.lme.com (accessed June 25th of 2013).
27. MetalPrices.com, http://www.metalprices.com (accessed June 25th of 2013).